PNAS
www.pnas.org

Supplementary Information for

Flame-formed carbon nanoparticles exhibit quantum dot behaviors

Changran Liu, Ajay V. Singh, Chiara Saggese, Quanxi Tang, Dongping Chen, Kevin Wan, Marianna Vinciguerra, Mario Commodo, Gianluigi De Falco, Patrizia Minutolo, Andrea D'Anna, Hai Wang

Corresponding author: Hai Wang
Email: haiwang@stanford.edu

This PDF file includes:

Supplementary text
Figs. S1 to S17
Tables S1 to S3
References for SI reference citations

www.pnas.org/cgi/doi/10.1073/pnas.1900205116

S1. Sample Preparation

Flame-formed carbon nanoparticles (CNPs) of several nanometers in size are sometimes called nascent soot (in contrast to mature soot that emits from a combustion process). The CNPs are prepared using two types of flames, the stagnation flame and burner-stabilized flame, both of which have the unburned gas mixtures premixed before they are issued through the burner. The stagnation flame is also called the (flow) stretch-stabilized flame. Details of the flames and sample preparation in each type of the flame are provided here.

S1.1. Premixed Stagnation Flames

CNPs prepared in premixed stagnation flames of ethylene (C_2H_4)-oxygen (O_2)-nitrogen (N_2) form the basis of our baseline, comprehensive studies. The experimental setup has been discussed elsewhere [1]. As Fig, S1*a* shows, the burner uses a diverging-straight tube-converging nozzle to produce a plug flow at the nozzle exit. The diameter at the nozzle exit is 1.43 cm. The flow impinges against a water-cooled aluminum disc, hereafter referred to as the stagnation surface. The flow issued from the nozzle thus forms a diverging, yet quasi-one dimensional flow [1]. The flame thus stabilized is disc-like owing to the nearly equal axial velocity of the flow as it is directed toward the stagnation surface and diverges radially outward (see, Fig. S1*b*). A shroud of nitrogen surrounds the center flow, insulating it from ambient air. The growth of the CNPs is intercepted by the limited reaction time, thus leading to the production of CNPs or nascent soot before it reaches maturity when it is collected on the stagnation surface. With this setup, it is possible to control and fine-tune the residence time of the particles beyond nucleation. The control allows us to prepare particle samples of small but different sizes by adjusting the cold flow velocity (v_0) and/or nitrogen dilution.

Table S1 lists the conditions of five series of ethylene flames. There are 15 flames in all. For each series of the flames, the nitrogen dilution in the unburned mixture is held fixed, whereas the cold gas velocity is varied, thus allowing for the adjustment of the flame standoff distance (L_s) or the residence time. The levels of nitrogen dilution provide changes in the reactant concentrations, and hence the CNP size to an extent.

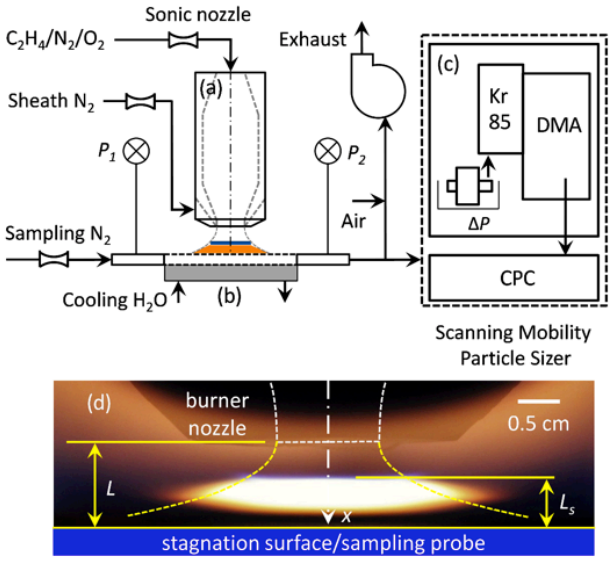

Fig. S1. Schematic showing various parts of the stagnation flame setup: (a) aerodynamically-shaped nozzle, (b) sampling probe/stagnation surface, and (c) Scanning Mobility Particle Sizer for mobility diameter measurements. (d) A typical flame image.

Maximum flame temperature $T_{f,max}$ may be evaluated by solution of a joint set of species and energy conservation with v_0, composition of the unburned gas and the temperatures of the gas at the nozzle exit T_n and at the stagnation surface T_s as the boundary conditions. T_n and T_s are measured using K-type thermocouples (125 μm wire diameter). Here, the evaluation of $T_{f,max}$ uses the OPPDIF code [2] and a chemical reaction model, USC Mech II [3].

Samples were also collected in several ethylene flames doped with kerosene or Jet A (Table S2). The liquid fuel is pre-vaporized in a vaporization chamber heated to 513 K. Carried by a flow of N_2, the kerosene is mixed with a C_2H_4-O_2-N_2 flow before it is issued through the nozzle into the flame. Details of the experimental setup can be found elsewhere [4].

Particle mobility size and its distribution is determined online using a horizontal dilution probe imbedded in the stagnation disc and a scanning mobility particle sizer (TSI 3080) [1]. For the ex situ analyses, including Transmission Electron Microscopy (TEM), UV-vis light absorption spectroscopy, photon-electron spectroscopy in air, and cyclic voltammetry, the samples were collected thermophoretically from the flames on quartz slides affixed on the stagnation surface for a duration of 1 min. Sensitivity of the absorbance to the sample size or the deposition time was tested over the deposition time range of 1 to 10 min. Details will be discussed in Section S4. Electrode preparation for cyclic voltammetry is discussed in section S5.

Table S1. Key ethylene stagnation flame parameters[a] and median diameter and geometric standard deviation of particles prepared therein.

Flame	v_o[b] (cm/s)	$T_n \pm 10$ (K)	$T_s \pm 5$ (K)	L_s[c] (mm)	$T_{f,max}$[d] (K)	$\langle D_{m,v} \rangle$ (nm)	$\sigma_{g,v}$	$\langle D_m \rangle$[e] (nm)	σ_g[e]
S1: 19.4% C_2H_4/ 24.3% O_2/ 56.3% N_2									
a	51	364	345	0.61	2122	5.2	1.19	4.6	1.17
b	61	382	365	0.54	2132	4.5	1.16	4.3	1.17
c	74	380	371	0.46	2131	3.9	1.16	3.5	1.18
S2: 17.6% C_2H_4/ 22.0% O_2/ 60.4% N_2									
a	29	417	350	0.77	2042	16.8	1.41	11.1	1.47
b	43	428	359	0.57	2052	12.1	1.39	8.5	1.43
c	51	443	369	0.52	2061	9.8	1.37	7.1	1.41
S3: 17.4% C_2H_4/ 21.7% O_2/ 60.9% N_2									
a	32	440	358	0.80	2010	20.5	1.42	12.7	1.51
b	44	409	336	0.54	2024	10.7	1.37	7.7	1.40
c	51	431	354	0.48	2038	10.2	1.38	7.3	1.40
S4: 17.3% C_2H_4/ 21.6% O_2/ 61.1% N_2									
a	35	355	311	0.56	1994	23.2	1.42	14.3	1.56
b	43	392	338	0.51	2019	16.3	1.41	10.8	1.48
c	46	424	361	0.52	2036	13.3	1.40	9.1	1.44
S5: 16.5% C_2H_4/ 20.6% O_2/ 62.9% N_2									
a	29	397	324	0.73	1973	21.8	1.51	12.6	1.54
b	43	388	334	0.59	1969	20.5	1.48	11.7	1.58
c	51	392	328	0.54	1971	16.5	1.49	10.2	1.49

[a]The equivalence ratio is 2.4. The nozzle-to-stagnation surface separation is 1 cm. [b]v_0 is the "cold" velocity of the unburned gas issued from the nozzle. The values listed are for 298 K and 1 atm, though the actual temperature is higher, as shown in the T_n column. [c]Distance from the stagnation surface to the position of $T_{f,max}$ [d] Modeled using OPPDIF [2] and USC Mech II [3]. [e] Median diameter and geometric standard deviation of the number size distribution are provided here for comparison. The volume median diameter $\langle D_{m,v} \rangle$ and its corresponding geometric standard deviation $\sigma_{g,v}$ are used as the relevant size parameters.

Table S2. Key Jet-A/C_2H_4 stagnation flame parameters[a] and median diameter and geometric standard deviation of particles prepared therein.

Flame	v_o[b] (cm/s)	$T_n \pm$ 10 (K)	$T_s \pm 25$ (K)	L_s[c] (mm)	$T_{f,max}$[d] (K)	$\langle D_{m,v} \rangle$ (nm)	$\sigma_{g,v}$	$\langle D_m \rangle$[e] (nm)	σ_g[e]
J1: 11500±15 PPM (mass) Jet A in 12.2%C_2H_4/17.8%O_2/70.0%N_2									
a	50.3	513	368	3.9	1890	5.8	1.30	4.5	1.33
b	45.2	513	368	4.2	1910	6.8	1.34	5.3	1.35
c	39.7	513	368	4.6	1910	8.5	1.36	6.4	1.45

[a]All unburned mixtures comprise of 12.2 % (mol) C_2H_4, 17.8% O_2, 70.0% N_2. 11500 PPM by mass of a kerosene is doped into the gas mixture. The overall equivalence ratio is 2.24. The nozzle-to-stagnation surface separation is 1 cm. [b]v_0 is the "cold" velocity of the unburned gas issued from the nozzle. The values listed are for 298 K and 1 atm, though the actual temperature is higher, as shown in the T_n column. [c]Distance from the stagnation surface to the position of $T_{f,\max}$. [d]Modeled using OPPDIF [2] and USC Mech II [3]. Median diameter and geometric standard deviation of the number size distribution are provided here for comparison. The volume median diameter $\langle D_{m,v} \rangle$ and its corresponding geometric standard deviation $\sigma_{g,v}$ are used as the relevant size parameters.

Table S3. Key ethylene burner-stabilized stagnation flame parameters and lognormal distribution parameters of particles prepared therein.

Flame	Mole fraction C_2H_4	O_2	Diluent	$T_{f,\max}$[a] (K)	HAB[b] (cm)	$\langle D_{m,v} \rangle$ (nm)	$\sigma_{g,v}$	$\langle D_m \rangle$[c] (nm)	σ_g[c]	Sample collection
BS1[d]: v_o = 10 cm/s (298 K, 1 atm), burner diameter = 6.0 cm										
a	12.0	18.5	69.5	1716±50	1.5	7.3	1.32	5.1	1.45	dilution probe
b	13.2	18.3	68.5	1678±50	1.5	21.3	1.61	9.9	1.69	
c	14.0	18.1	67.9	1633±50	1.5	25.7	1.51	15.2	1.56	rapid
d	15.2	17.9	67.0	1527±50	1.5	64.5	1.43	29.1	1.71	insertion
BS2[d]: v_o = 10 cm/s (298 K, 1 atm), burner diameter = 5.6 cm										
a	13.0	18.3	68.7	1730±50	0.5	2.4[e]	1.18[f]	2.2[e]	1.17[e]	
b	13.0	18.3	68.7	1730±50	0.6	2.6[e]	1.18[f]	2.4[e]	1.18[e]	in situ
c	13.0	18.3	68.7	1730±50	0.8	3.0[e]	1.20[f]	2.7[e]	1.20[e]	light
d	13.0	18.3	68.7	1730±50	1.1	6.2[e]	1.30[f]	5.0[e]	1.29[e]	absorption
e	13.0	18.3	68.7	1730±50	1.2	7.9[e]	1.34[f]	6.3[e]	1.32[e]	
BS3[g]: v_o = 8 cm/s (298 K, 1 atm), burner diameter = 5.0 cm										
a	16.3	23.7	60.0	1850±87	0.7	8.5	1.29	7.1	1.29	
b	16.3	23.7	60.0	1872±87	0.8	11.8	1.36	8.5	1.39	cooled
c	16.3	23.7	60.0	1852±84	1.0	14.8	1.44	9.4	1.46	quartz
d	16.3	23.7	60.0	1860±87	1.2	20.2	1.47	11.4	1.58	slide
e	16.3	23.7	60.0	1874±88	1.5	25.3	1.50	13.1	1.61	
f	16.3	23.7	60.0	1876±88	2.0	29.3	1.52	13.8	1.64	

[a] Measured maximum flame temperature. [b] Height above the burner (HAB) over which the soot sample is collected/measured in BS1 and BS2 series and the burner-to-stagnation separation distance of the BS3 series. [c]Median diameter and geometric standard deviation of the number size distribution are provided here for comparison. The volume median diameter $\langle D_{m,v} \rangle$ and its corresponding geometric standard deviation $\sigma_{g,v}$ are used as the relevant size parameters. [d]University of Naples. Nitrogen is used as the diluent. [e]Based on light extinction and scattering ($D_{6\text{-}3}$) measurement and modeled assuming the size distribution is log-normal. [f]Estimated using Eq. **S2**. See section S2. [g]Stanford University. Argon is used as the diluent.

S1.2 Premixed Burner-Stabilized (BS) Flames

Three burners are used to prepare CNP samples in three series of flames with similar flame conditions but with different sample collection methods. University of Naples used burners of two different sizes (a McKenna burner 6 cm in diameter and a capillary burner 5.6 cm in

diameter). Stanford uses a home-made burner 5 cm in diameter. All of the flames were operated at atmospheric pressure. Table S3 lists the conditions of these flames. Fig. S2 shows the schematics of the experimental setup of the BS1 and BS2 series of flames. A stainless steel plate 0.4 cm in its thickness is positioned at 2.8 cm from the burner surface for flame stabilization. The particles are all prepared in C_2H_4-O_2-N_2 flames with a cold gas velocity of 10 cm/s (298 K & 1 atm). For BS1 sample series, two methods were used for sample collection. The BS1a sample was extracted from the centerline of the flame using a horizontal tubular dilution probe in which the flame gas enters into an orifice 0.25 cm in diameter and is rapidly diluted with N_2 at a dilution ratio of 3000. The particles are collected online on a quartz slide positioned inside a stainless-steel filter holder maintained at 350 K downstream of the probe. For BS1-b, -c, and -d, the particles are captured thermophoretically on a 7.5 × 2.5 × 0.1 cm quartz slide by inserting it horizontally into the flame using a compressed-air piston. The duration of each insertion is 0.1 s, after which the slide is retracted from the flame, allowing it to cool in ambient air for 10 s before the next insertion. The procedure is repeated up to 300 insertions or until a desirable amount of material is collected. Properties measured are found to be independent of the number of insertions or the sample size. BS2 series flames use in situ laser light scattering and UV-visible light absorption to determine particle size and optical band gap, respectively. Details will be provided in S4. For BS3 series of the flames, the particle samples were collected on 7.5 × 2.5 × 0.1 cm quartz slides affixed to a water-cooled disc in a manner like the S1-S5 series of samples. The collection time is also fixed at 1 min.

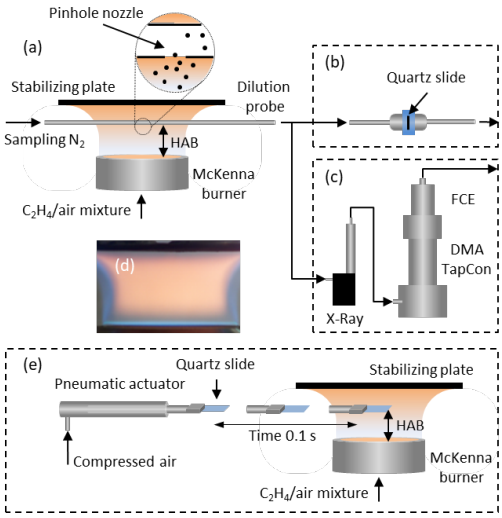

Fig. S2. Schematics showing the setups for (a) flame and the dilution probe sampling, (b) on-line particles collection on a quartz slide for the BS1-a flame, (c) differential mobility analysis set-up, (d) a typical BS flame image (e) BS1-b thru g flames and the method of sample collection by rapid insertion.

S2. Particle Sizes and Their Distributions

CNP size distribution functions (PSDFs) of all stagnation flames were measured by electric mobility sizing [1]. Flame samples were collected at the stagnation surface in situ into a micro-orifice on the probe tube imbedded in the stagnation disc. The probe was connected to an SMPS system (TSI3090) for mobility size measurement (see Fig. S1). Considering the limitation of the empirical Cunningham slip correction for mobility diameter for particles smaller than 10 nm, mobility size correction was performed following a procedure documented elsewhere [5]. In the particle size range of interest, mobility sizing is based on the measurement of the cross section

area of a particle [6, 7]. Hence, the sphericity assumption is inherently imbedded in mobility sizing when the cross section area is converted to an equivalent spherical radius or diameter for a cross section. For small CNPs, sphericity as an assumption is commonly used in nearly all related research work thus far. Fig. S3*a* shows the mobility size distributions of the 15 base premixed stagnation flames (see Table S1). Because all of the properties studied herein are related to sample size, which is measured by particle volume, we present the volume fraction (V) distribution with respect to the particle size. The volume distribution $dV/d\log(D_m)$ is related to the commonly used number distribution. i.e., $(\pi D_m^3/6)\ dN/d\log(D_m)$. The observed particle volume distribution is well described by the lognormal distribution function, as shown by the solid lines in Fig. S3*a*,

$$\frac{dV}{d\log D_m} = \frac{V}{\sqrt{2\pi}\log\sigma_{g,v}} \exp\left[-\frac{\left[\log D_m - \log\left\langle D_{m,v}\right\rangle\right]^2}{2\left(\log\sigma_{g,v}\right)^2} \right], \qquad \textbf{[S1]}$$

where $\sigma_{g,v}$ is the geometric standard deviation and $\langle D_{m,v}\rangle$ is the median mobility diameter. The values of both size parameters are provided in Fig. S3*a* and Table S1. As discussed in the main text, the $\langle D_{m,v}\rangle$ values are used as the size parameter for characterizing the size dependency of the ionization energy and band gap. As shown in Table S1 and Fig. S3*a*, the median particle diameter ranges from 3.9 to 23.2 nm. The geometric standard deviation for the larger particles is quite close to 1.45 that is characteristic of a self-preserved distribution [8]. As expected, the particle size increases with an increase in the flame standoff distance within each series of the flames and with a reduced nitrogen dilution across the five flame series.

The measured mobility size was verified by TEM size analysis. An FEI Tecnai G2 F20 X-TWIN Transmission Electron Microscope operating at 200 keV was used for this purpose. The images were processed and analyzed in ImageJ for the determination of the primary particle size distribution. In obtaining the TEM-derived size distributions, we ensured that the sizing method is consistent with the mobility measurement. Since mobility sizing measures the cross section area of a particle, we used ImageJ to first trace the edge of an imaged, primary particle by a 2-D ellipse. This projection area is then calculated and the equivalent spherical diameter is determined for the particle. Representative results have been presented in Fig. 1*c* of the paper. To show that the sphericity assumption inherent to the mobility size determination does not notably impact the actual size determination, we plot in Fig. S4 the aspect ratio of the particles as imaged by TEM for sample 4a. Sample 4a has the largest particle size among the S1 thru S5 series of the samples, so the aspect ratio plotted represents the worst-case scenario of departure from sphericity among the S1-S5 samples tested. Smaller primary particles usually have smaller departure from sphericity [9, 10]. As it can be seen, most of the particles are within the aspect ratio of 1.2. The distribution gives a mean aspect ratio of 1.19. For this worst-case senario, the spherical volume differs from the actual volume by 9% on average if the particles are treated geometrically as a prolate spheroid, as explained in Fig. S4. The equivalent particle diameter difference is only 3%, which is much smaller than the geometric standard deviation of 1.42 for the same sample. Hence, the sphericity assumption produces negligible error as far as particle size is concerned.

The close agreement between the mobility size and the primary particle size as measured by TEM further indicates that the particle sizing methods used here generate expected, consistent results, and as such it is apprproate to use the size data for characterize the quantum confinement effect in the ionization energy and the optical band gap. This agreement also indicates that the aggregate structure of the particle sample shown in Fig. 1 is the result of particle aggregation during the sample is collected. In the flames and before the particles are collected, the particles are largely single, primary particles of sizes as measured by mobility.

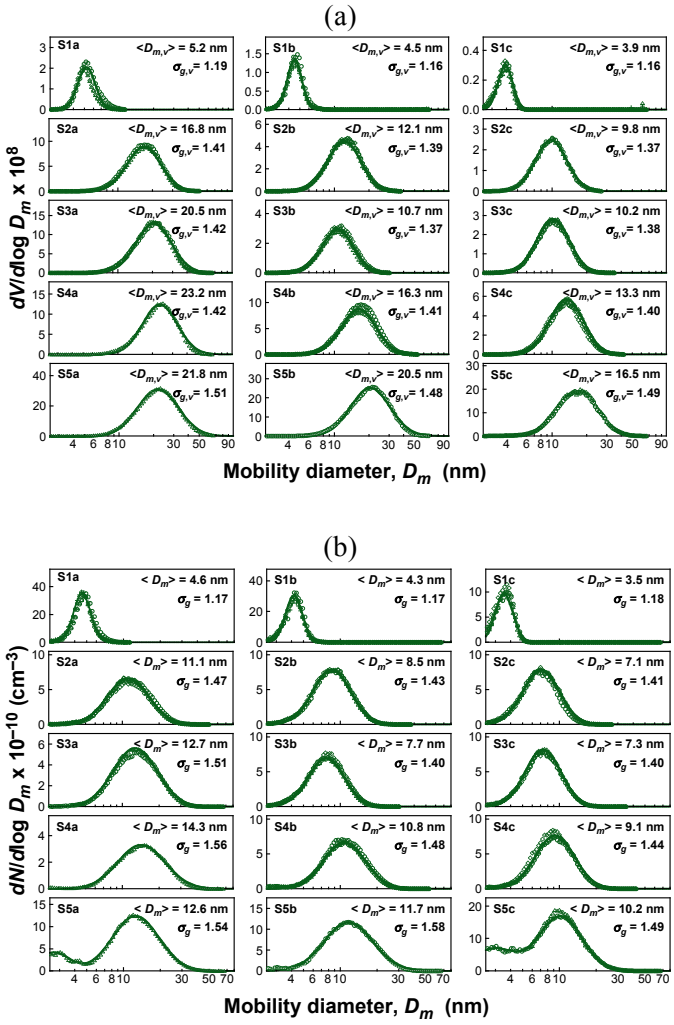

Fig. S3. (a) Particle volume fraction distributions and (b) particle number distributions of the S1-S5 series of CNPs. Symbols are experimental data; lines are lognormal fits to data. In the number distribution plots, S5a and S5c used the bi-lognormal distribution function.

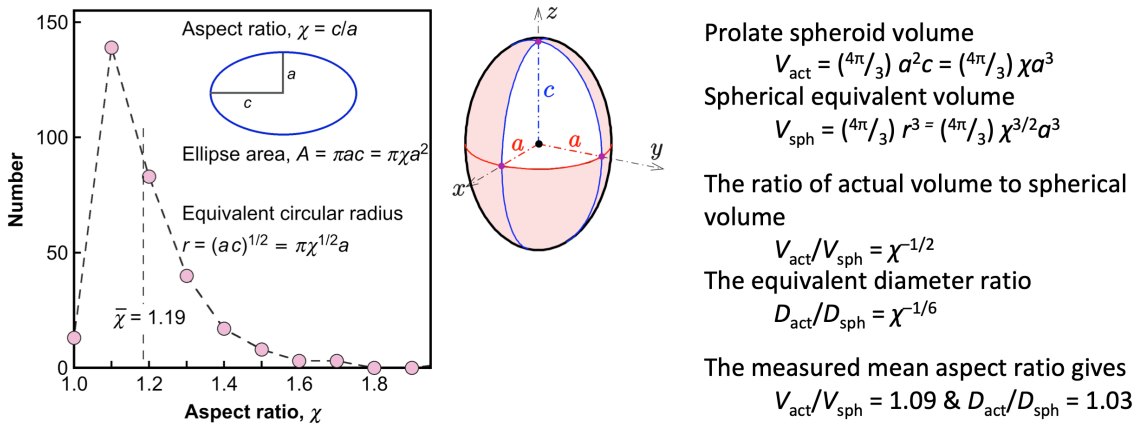

Fig. S4. Histogram of the aspect ratios measured for the 2-D projection of primary particles of the S4a sample, measured by TEM.

As shown in Fig. S5, high-resolution TEM image on the S4c sample indicates that the CNPs are characterized by often a concentric organization of the stacked molecular layers, which is presumably polycyclic aromatic hydrocarbon (PAH) in nature. The particles appear as somewhat ordered carbon with extended PAH layers, each with some degree of curvature. The mean fringe length was found to be 0.83 ± 0.2 nm. Because the sample is exposed to incoming flame gas after it is deposited on the quartz slide, there is no evidence of aging from the absorbance measurement, as will be discussed later, probably because the stagnation surface and hence the substrate was water-cooled.

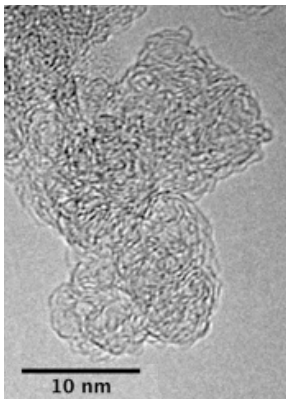

Fig. S5. A typical TEM image of the CNP sample (S4c).

The PSDFs of CNPs from flame series J1 (Table S2) and series BS1 and BS3 (Table S3) are determined in a fashion similar to those of the ethylene stagnation flames just discussed, either in the present study or in earlier, separate studies [4, 11]. While the mobility measurement at Stanford was carried out using the TSI3090 system, that at the University of Naples used a differential mobility analyser (DMA TapCon 3/150) equipped with a Soft X-ray neutralizer (TSI3088) and a Faraday cup electrometer detector. For the BS1 series, particle samples were withdrawn into a horizontal probe through a micro-orifice positioned horizontally in flame. Nitrogen was used as the diluent and carrier gas with the dilution ratio equal to 3000 [12]. PSDFs are shown in Figs. S6*a*, S7*a*, and S8*a* for J1, BS1 and BS3 series of the samples, respectively, where the size parameters were obtained in a manner identical to those of Fig. S3*a*. Some of the size distributions are bimodal (e.g., BS3a thru BS3c) with a shoulder appearing toward the small particle size. These small particles are not expected to impact the ionization energy or band gap because their number and mass contributions are small. The bimodal distributions are fitted as a sum of two lognormal functions with the size parameters of the large size mode shown and used in the apparent quantum confinement analysis.

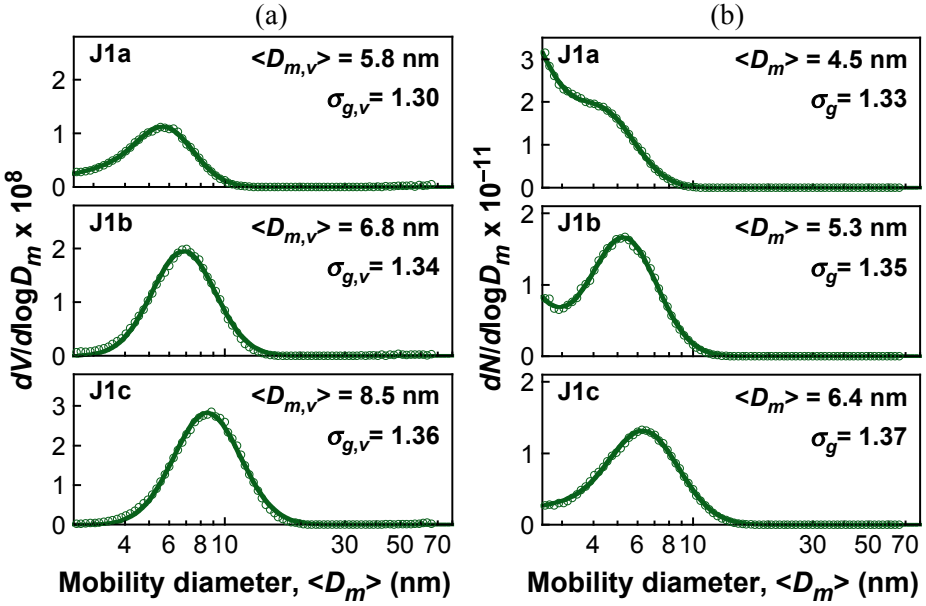

Fig. S6. (a) Mobility volume fraction distributions and (b) mobility number distributions of the J series of particle samples. Symbols are experimental data, lines are lognormal fits to data. The number distributions use bi-lognormal distribution functions.

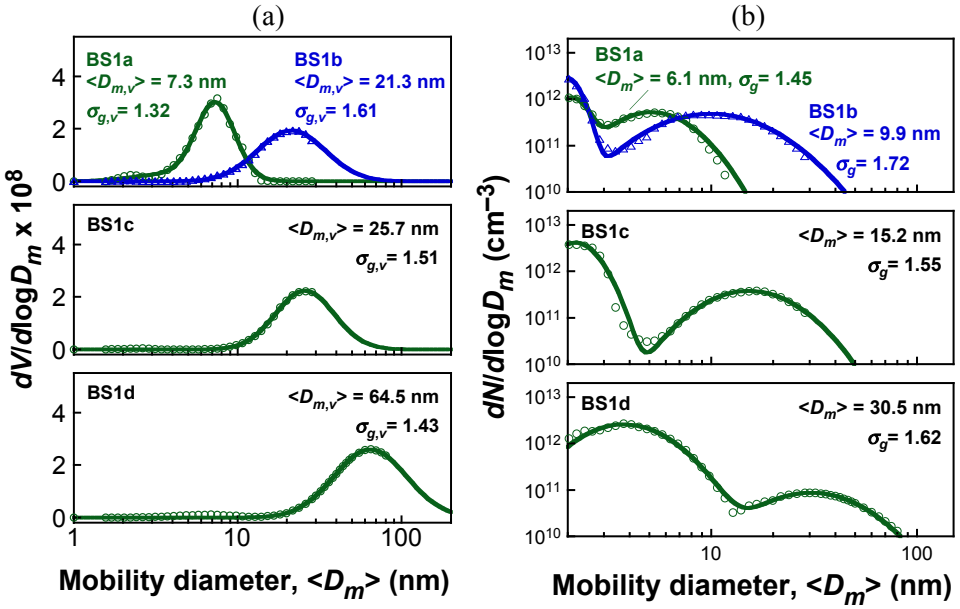

Fig. S7. (a) Mobility volume distributions and (b) mobility number distribution of particles of the BS1 series of samples. Symbols are experimental data, lines are lognormal fits to data. The number distributions use bi-lognormal distribution functions.

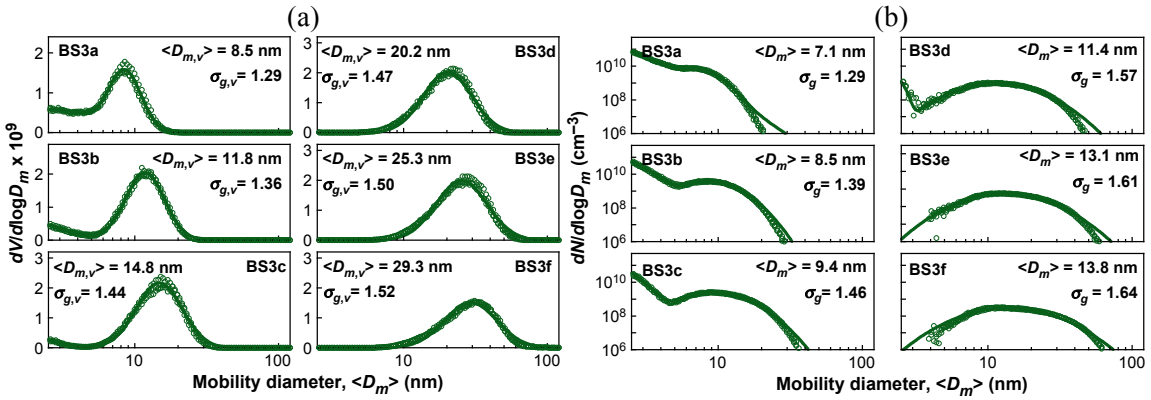

Fig. S8. (a) Mobility volume fraction distributions and (b) mobility number distribution of the BS3 series of particle samples. Symbols are experimental data, lines are lognormal fits to data. The number distributions use bi-lognormal distribution functions, where appropriate.

The size parameters for the PSDFs of Figs S3*a*, S6*a*, S7*a* and S8*a* are highly correlated, as shown in Fig. S9. The correlation may be given empirically by

$$\sigma_{g,v} = 1.52 - 0.44\exp\left(-0.104\left\langle D_{m,v}\right\rangle\right). \qquad \textbf{[S2]}$$

The sizes of BS2 series of particles were obtained by in situ light scattering and absorption following the approach already discussed in [13-15]. With the assumptions that particles are spherical and follow Rayleigh scattering, the ratio of the light scattering and absorption coefficients is proportional to the ratio of the 6th to 3rd moment of the size distribution, $D_{6\text{-}3}$ [16] at a given wavelength λ is

$$\frac{Q_{vv}(\lambda)}{K_{ext}(\lambda)} = -D_{6\text{-}3}^{3}\pi^{2}\left|\frac{m^{2}-1}{m^{2}+1}\right| \Bigg/ \left[4\lambda^{3}\,\mathrm{Im}\left(\frac{m^{2}-1}{m^{2}+1}\right)\right], \quad \textbf{[S3]}$$

where $K_{ext}(\lambda)$ and $Q_{vv}(\lambda)$ are the wavelength-dependent extinction and scattering coefficients, respectively, and m is the complex refractive index $m = n - ik$. The $D_{6\text{-}3}$ values thus obtained were converted to the median diameter of the volume distribution by modeling the number distribution as a longnormal function with the geometric standard deviation estimated using Eq. **S2**. This procedure is supported by previous investigations showing a direct comparison of size distribution obtained by mobility, AFM and that retrieved by light scattering/absorption [14, 17].

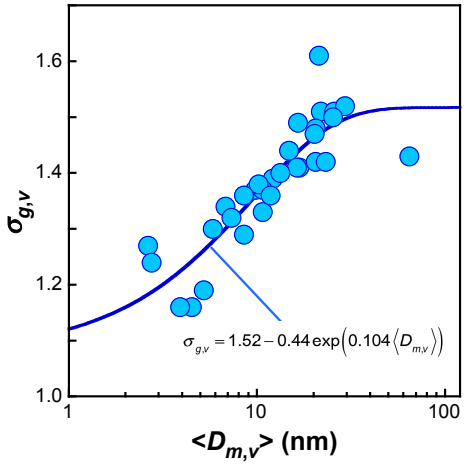

Fig. S9. Correlation between geometric standard deviation and median diameter of lognormal volume distributions. Symbols are fitted values in Figs. S3, and S6 thru S8; line is fit to the data (Eq. **S2**).

In the measurement, the fourth harmonics of a Nd: Yag pulsed laser (λ = 266 nm, vertically polarized) was used for the Q_{vv} determination. The vertically polarized component of the scattered light was selected by a polarization analyzer and focused on the entrance slit of the spectrometer coupled to an ICCD camera detection system. The signal was calibrated by measuring the scattering from methane at ambient temperature, whose cross section is known from literature. Correction of the scattering from gas phase species was made to obtain the particle light scattering coefficient. For light extinction measurements, the light emitted by a high-temperature plasma was sent through the flame and detected in the wavelength range of 200-600 nm by a spectrometer/ICCD detection system. The flame-background was subtracted from the recorded signal. The extinction spectra attributed to particles were obtained by subtracting the calculated extinction expected from CO_2 and H_2O at the flame temperature [18]. The refractive index value was taken from Ref. [19].

When the median diameter of a lognormal number distribution $\langle D_m \rangle$ is the only known size parameter, like the CAST1 soot [20] discussed in the main text, the $\langle D_{m,v} \rangle$ value is estimated by modeling the number distribution using the geometric standard deviation evaluated by Eq. **S2** in an iterative manner. Suffice it to note that the geometric standard deviation of the number distribution is nearly the same as the volume distribution.

In Figs S3 and S6 thru S8, we also present the number density distributions (panels *b*). The median particle diameter $\langle D_m \rangle$ is extracted from the measured number distribution and listed in Tables S1 thru S3 for each sample. $\langle D_m \rangle$ is smaller than the corresponding volume median diameter $\langle D_{m,v} \rangle$, as one would expect. In many cases, bimodal number distributions are observed and the cause for the bimodality has been discussed in many early publications (e.g., [1, 11]). A bi-lognormal distribution functions is used to describe such distribution. In such cases, the $\langle D_m \rangle$ value refers to the median diameter of the large size mode in a bimodal distribution. It will be shown in section S5 that the choice of $\langle D_m \rangle$ and $\langle D_{m,v} \rangle$ does not impact the conclusion of the current study.

S3. Treatment of Size Distribution Effect

S3.1. Quantum Confinement

The Brus theory [21] was originally derived to explain the size dependency of the optical band gap. The shifts in the conduction and valance bands were approximated by solving the first non-zero term of the Taylor expansion of the electron energy band in a spherical cluster. The optical band gap is given as

$$E_g^{opt}\left(D\right) \cong E_{g,\infty}^{opt} + \frac{h^2}{2m_0 D^2}\left(\frac{1}{m_e^*} + \frac{1}{m_h^*}\right) - \frac{1.8e^2}{2\pi\varepsilon_0\varepsilon_s D}, \qquad \textbf{[S4]}$$

where $E_{g,\infty}^{opt}$ is the bandgap of the bulk material, e is the elementary charge, ε_0 is the permittivity of the vacuum and ε_s is the relative permittivity of the particle material, m_e^* and m_h^* are the effective electron and hole masses, respectively, m_0 is the electron rest mass, and D is the particle diameter. The second term of the above equation accounts for the quantum confinement effect due to an elevated valance band edge and a lowered conduction band edge as the size decreases. The third term accounts for the Coulomb electron-hole interaction. Because the particle samples studied herein are polydispersed, we assume that the mobility diameter D_m can be used to represent the diameter in Eq. **S4**, and thus, the ensemble-averaged, apparent band gap of a polydispersed CNP sample may be expressed by

$$\left\langle E_g^{opt}\right\rangle \cong E_{g,\infty}^{opt} + \frac{h^2}{2m_0}\left(\frac{1}{m_e^*} + \frac{1}{m_h^*}\right)\left\langle\frac{1}{D_{m,v}^2}\right\rangle - \frac{1.8e^2}{2\pi\varepsilon_0\varepsilon_s}\left\langle\frac{1}{D_{m,v}}\right\rangle, \qquad \textbf{[S5]}$$

where the l^{th} moments of the volume distribution:

$$\begin{aligned}\left\langle D_{m,v}^l\right\rangle &= \frac{1}{2}\frac{\int_{-\infty}^{\infty}\left(D_m\right)^l\left(dV/d\log D_m\right)d\log D_m}{\int_{-\infty}^{\infty}\left(dV/d\log D_m\right)d\log D_m} \\ &= \left(\left\langle D_{m,v}\right\rangle\right)^l \exp\left[\frac{1}{2}\left(\ln\sigma_{g,v}^l\right)^2\right]\end{aligned}. \qquad \textbf{[S6]}$$

For the current study, we have $l = -1$ or -2.

S3.2. Size Effect on Ionization Energy in Air

In photoelectron emission, incident photons cause emissions of electrons from the top of the valance band of the material. The ionization energy can be divided into two parts. The first part is due to electron excitation from the top of the valence band to the bottom of the conduction band; and its size dependency can be evaluated using the second term of Eq. **S4** except that the exciton mass is replaced by the hole mass. The second part allows the electron to overcome the Coulomb attraction leading to emission of electron into the air; and the size dependency is caused by the polarization image charge. The emitted electrons near the particle surface induce polarization charges on the particle. The interaction between the emitted electron and the image charge varies with the particle size. Induced image charge potential has been studied for metal particles by Seidl [22]. In current work, the polarization charge effect is treated as

$$\Sigma_e^{pol} = \frac{e^2}{4\pi\varepsilon_0 D}\left(\frac{1}{\varepsilon_{air}} - \frac{1}{\varepsilon_s}\right), \qquad \textbf{[S7]}$$

where ε_{air} is the relative permittivity of air. Electrons are emitted into the air and they are subject to the electron-hole Coulomb interaction. Hence, the ionization energy may be given as

$$E_i\left(D\right) = E_{I,\infty} + \frac{h^2}{2m_0 m_h^* D^2} + \frac{e^2}{4\pi\varepsilon_0 D}\left(\frac{1}{\varepsilon_{air}} - \frac{1}{\varepsilon_s}\right), \qquad \textbf{[S8]}$$

where $E_{i,\infty}$ is the ionization energy of the bulk material. In this manner, the size dependency of the ionization energy arises from the shift of the valance band due to quantum confinement (the

second term of Eq. **S8** and polarization charge potential (the third term). Again, Eq. **S8** may be ensemble-averaged over the particle volume distribution as

$$\left\langle E_i \right\rangle \left(D_{m,v} \right) = E_{i,\infty} + \frac{h^2}{2m_0 m_h^*} \left\langle \frac{1}{D_{m,v}^2} \right\rangle + \frac{e^2}{4\pi\varepsilon_0} \left(\frac{1}{\varepsilon_{air}} - \frac{1}{\varepsilon_s} \right) \left\langle \frac{1}{D_{m,v}} \right\rangle, \qquad \textbf{[S9]}$$

S3.3. Determination of Ionization Energy in Air of a Polydispersed Particle Ensemble

For a polydispersed particle ensemble, the measured photoemission yield is understood as the ensemble average of particle-size specific yield $y(\upsilon, D_m)$ at a given photon frequency υ,

$$\left\langle Y\left(\upsilon\right) \right\rangle = \int_{-\infty}^{\infty} y\left(\upsilon, D_m\right) \left(\frac{dV}{d\log D_m} \right) d\log D_m, \qquad \textbf{[S10]}$$

where $\langle Y(\upsilon) \rangle$ is the ensemble-average photoemission yield. Applying $y^{1/2} = h\upsilon - E_i$ to Eq. **S10** and rearranging the terms, we can express the photoemission yield as,

$$\left\langle Y\left(\upsilon\right) \right\rangle = \left[\left(h\nu - \left\langle E_i \right\rangle \right)^2 + \left\langle \left(E_i - \left\langle E_i \right\rangle \right)^2 \right\rangle \right], \qquad \textbf{[S11]}$$

where $\langle E_i \rangle$ is the volume-weighted mean ionization energy of the particle ensemble, i.e.,

$$\left\langle E_i \right\rangle = \int_{-\infty}^{\infty} E_i\left(D_m\right) \left(\frac{dV}{d\log D_m} \right) d\log D_m, \qquad \textbf{[S12]}$$

and $\langle (E_\mathrm{i} - \langle E_i \rangle)^2 \rangle$ is the variance given by

$$\left\langle \left(E_i - \left\langle E_i \right\rangle \right)^2 \right\rangle = \int_{-\infty}^{\infty} \left(E_i - \left\langle E_i \right\rangle \right)^2 \left(\frac{dV}{d\log D_m} \right) d\log D_m. \qquad \textbf{[S13]}$$

The above variance is estimated to be < 0.1 eV^2, which is much smaller than the first term in Eq. **S11**. Hence, Eq. **S11** may be reduced to

$$\left\langle Y\left(\upsilon\right) \right\rangle^{1/2} \cong h\nu - \left\langle E_i \right\rangle. \qquad \textbf{[S14]}$$

The ionization energy $\langle E_i \rangle$ may be determined from an extrapolation of $\langle Y(\upsilon) \rangle^{1/2}$ to zero as shown in the inset of Fig. 2 of the main text.

S4. UV-Vis Absorption

Ex situ UV-vis absorption measurements were carried out on S1-5, J1, BS1 and BS3 series of samples using a Shimadzu UV-2401 PC spectrometer over the wavelength range of 185 to 1400 nm, and on the BS1 series using an Agilent UV–Vis 8453 spectrophotometer over the same wavelength range. Following Mott and Davis [23], the absorbance measured is analyzed to yield the optical band gap for each sample. Fig. S10*a* shows the absorbance curves of several samples; Figs S10*b* and S10*c* present their corresponding Tauc analyses, in which a plot of $(\alpha h\upsilon)^{1/k}$ versus $h\upsilon$ yields the optical band gap value $\left\langle E_g^{opt} \right\rangle$ by extrapolating the linear portion of the curve in the long wavelength range to zero $(\alpha h\upsilon)^{1/k}$, where α is the absorbance, h is the Planck constant. As discussed in Ref. [24], in absence of exciton, $k = 2$ is for allowed transition an indirect band gap material (Fig S10*b*) and $k = 1/2$ for allowed transition in a direct band gap material (Fig. S10*c*). As seen, the data clearly indicate the indirect transition behavior for the CNPs tested. Although a linear section could be defined for $k = ½$, the resulting band gap would be too high (e.g., ~ 4 eV for the S3b sample) for a material that is black in appearance in the sunlight.

Sample-size as measured by sample film thickness is found not to impact the determination of the apparent optical band gap, as shown in Fig. S11. The deposition time tested ranges from 1 min to 10 min. The absorbance increases with an increase in the deposition time or sample film thickness (Fig S11*a*), but the band gap values following Tauc analysis using $k = 2$ are seen to be independent of the film thickness (Fig S11*b*). In all subsequent tests, the deposition time was held fixed at 1 min. Previously, we used the same technique to characterize the optical band gap of flame-synthesized rutile and anatase TiO_2 nanoparticles [25]. The resulting optical band gap values where found to be in close agreement with literature values.

The particle size has notable effect on the band gap, as seen in Fig. S10*b*. An increase in particle size causes the band gap value to decrease. Depending on the particle size, the spectral feature over the range tested can be quite different. For the smallest particle size shown ($\langle D_{m,v} \rangle = 4.5$ nm), the absorbance drop to zero at around 1.6 eV, whereas the absorbance for $\langle D_{m,v} \rangle = 10.7$ nm is similar to that of $\langle D_{m,v} \rangle = 4.5$ nm, but a long tail appears at $hv < \sim 2$ eV. The variations of the spectral features are currently not well understood. Such a study is beyond the scope of the present work, as we are primarily interested in the apparent band gap of the CNP materials. Nonetheless, the spectral features and their variations with particle size deserve some further studies.

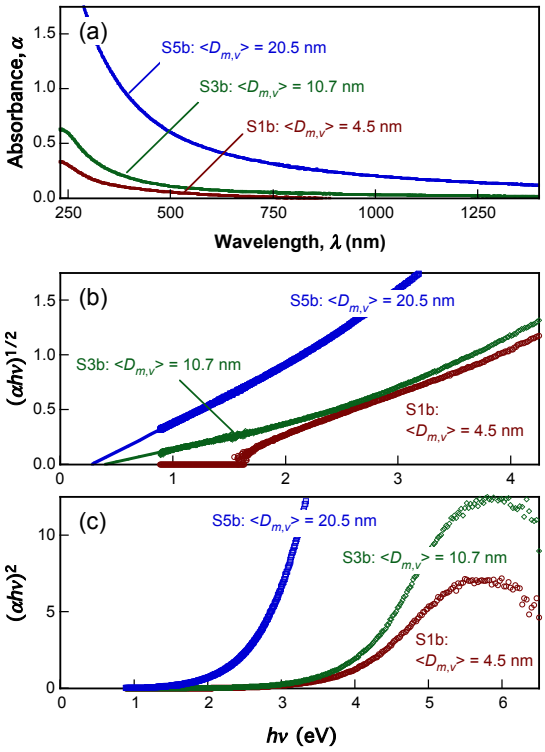

Fig. S10. (a) Typical absorbance curves measured, (b) Tauc analyses using $k = 2$, (c) Tauc analyses using $k = ½$.

The band gap values of the BS2 series were obtained in situ by laser absorption. A sketch of the experimental set up is reported in Ref. [26]. A Nd: Yag pulsed laser source was used to produce a broadband light; the first harmonics of the laser ($\lambda = 1064$ nm) with energy of 200 mJ was focused by a short focal lens to generate a high-temperature plasma by optical breakdown of air at the focal point. The induced plasma emitted a continuous, unstructured spectrum from the visible to the far ultraviolet with a time duration of tens of nanoseconds [27]. The light from the plasma was sent through the flame and detected in the wavelength range of 200 to 600 nm by a spectrometer coupled to an intensified and gated CCD camera. The flame-background was subtracted from the recorded signal. Fig. S12*a* shows the absorption spectra of the two representative BS2 samples, along with the corresponding Tauc analysis of the absorbance spectra. The linear region is quite well defined, allowing for extraction of the optical band gap values, as can be seen in Fig. S12*b*.

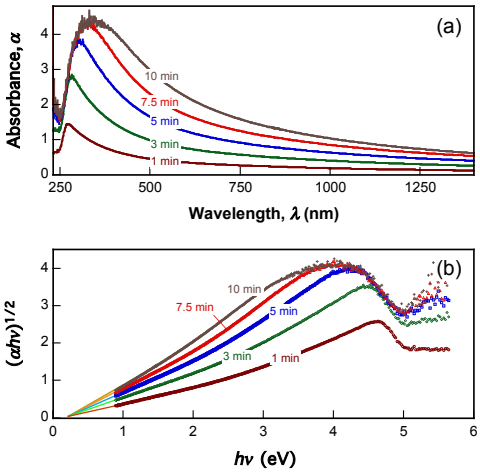

Fig. S11. Absorbance spectra (a) and Tauc analyses of the absorbance (b) of samples collected from the S4a flame with different sample sizes, measured by the film deposition time.

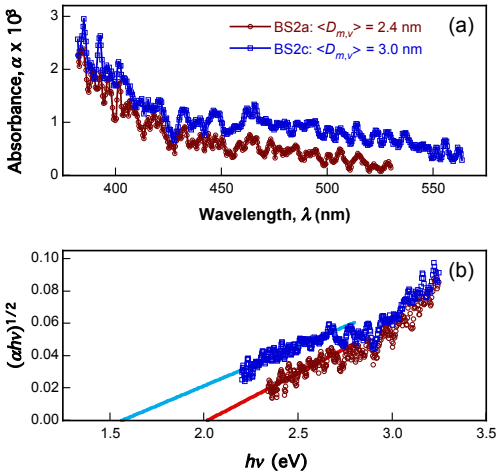

Fig. S12. Selected absorbance spectra by in situ light absorption of BS2 series of the samples. (a) Absorbance curves, (b) Tauc analysis of the absorbance.

S5. $\langle D_m \rangle$ Versus $\langle D_{m,v} \rangle$

As discussed in section S3, both the optical band gap and ionization energy are sensitive more directly to particle volume than the particle number. Hence the median particle diameter derived from the volume distribution ($\langle D_{m,v} \rangle$) is used as the size parameter in our analysis. On the other hand, the use of the median particle diameter from number distribution ($\langle D_m \rangle$) as the size parameter does not impact the conclusion of the current study. That is, the measured ionization energy and optical band gap can be still described closely by the quantum confinement effects given in Eqs. 1 and 4, respectively. To illustrate this point, we plot in Fig. S13 the ionization energy and optical band gap as a function of $\langle D_m \rangle$, both of which are fitted with the appropriate equations. As it can be seen, the use of $\langle D_m \rangle$ as the size parameter merely shifts the curves to somewhat smaller particle sizes; and compared to the use of $\langle D_{m,v} \rangle$, the parameters that are impacted are only the effective electron and hole masses.

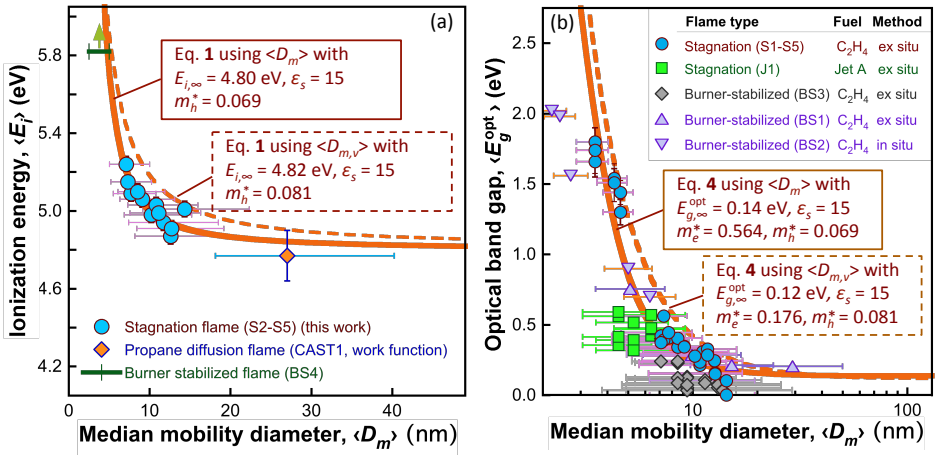

Fig. S13. Observed quantum size confinement effect in (a) ionization energy and (b) optical band gap, both using $\langle D_m \rangle$ as the size parameter. Symbols are experimental data. Solid lines: fit to data (using $\langle D_m \rangle$ as the size parameter). Dashed line in panel (a): from Fig. 2 of the main text using $\langle D_{m,v} \rangle$, and panel (b): from Fig. 4 of the main text also using $\langle D_{m,v} \rangle$ as the size parameter.

S6. Cyclic Voltametry

Cyclic voltametry (CV) curves were recorded on an electrochemical workstation (Gamry Interface 1000). We used a 3.0 mm diameter Pt disk as the working electrode, Pt wire as the counter electrode, and the Accumet Ag/AgCl, prefilled with 4 M KCl saturated with AgCl, as reference electrode. As the electrolyte, tetrabutylammonium hexafluorophosphate (TBAPF6) was dissolved in acetonitrile at 0.1 M concentration. The particle sample is coated onto the working electrode using a paste of the CNP sample in dichloromethane.

As discussed by Liu et al. [28], electrochemical band edge are directly related to the onset of redox potentials. The relationship between the band edge energy and the redox potentials can be described by

$$E_i^{EC} = E_{ox} + E_{ref}, \qquad \textbf{[S15]}$$

$$EA = -\left(E_{re} + E_{ref}\right), \qquad \textbf{[S16]}$$

where E_{ox} and E_{re} are the oxidation and reduction potentials, respectively, E_i^{EC} is the electrochemical ionization potential and EA is the electron affinity. In the above equation, E_{ref} is the reference electrode potential (relative to vacuum). We used ferrocene (0.02 M in acetonitile) to calibrate the potential of the reference electrode, which yield a E_{ref} value of 4.32 eV, independent of the voltage scan rate.

We tested several potential causes for measurement inaccuracies. Fig. S14 shows the influences of dissolved oxygen in electrolytic solution and the condition of the working electrode on blank CV measurements. We compared the CV curves without nitrogen purging and with nitrogen purging for 10 min before each experiment in Fig. S14*a*. The difference illustrates the importance of removing oxygen in the electrolyte and keeping the electrolyte anaerobic. The condition of the working electrode is another factor critical to a reliable CV measurement. Before each experiment, the electrode was cleaned using a concentrated nitric acid solution followed by rinsing in deionized water and drying in a nitrogen flow. We find, however, it is necessary to thoroughly polish the electrode using a fine grit sandpaper before the acid treatment. Fig. S14*b* illustrates the CV curve difference with and without this treatment. We adopted a voltage scan rate of 400 mV/s for the measurement. The voltage scan rate was carefully checked to ensure that the effect of overpotential is negligible. As illustrated in Fig. S15, the scan rate at or below 400 mV/s presents a negligible effect on the measured oxidation potential.

Fig. S16*a* depicts cyclic voltammograms of a CNP sample over three cycles. Each scan starts at zero potential vs. Ag/Ag^+. As the voltage is increased, the combined voltage applied to the CNP material and the energy level of its highest occupied molecular orbital (HOMO) increases. When this combined energy exceeds the Fermi level of the reference electrode, it creates a current into the working electrode. The voltage at the onset of the current characterizes the oxidation potential E_{ox} of the CNP material tested. After reaching the maximum set voltage of 2.5 V, the voltage is decreased. The combined voltage applied to the CNP material and the energy level of its lowest unoccupied molecular orbital (LUMO) decreases. When this combined energy level is below the Fermi level of the reference electrode, it creates a current out of the working electrode into the counter electrode. The voltage at the onset of the current is the reduction potential of the CNP material. Because of reduction and oxidation potentials are related to the LUMO and HOMO energy levels, respectively, the sum of the two ensemble averaged potentials yields the electrochemical band gap, i.e.,

$$\left\langle E_g^{EC} \right\rangle = \left\langle E_i^{EC} \right\rangle + \left\langle EA \right\rangle. \qquad \textbf{[S17]}$$

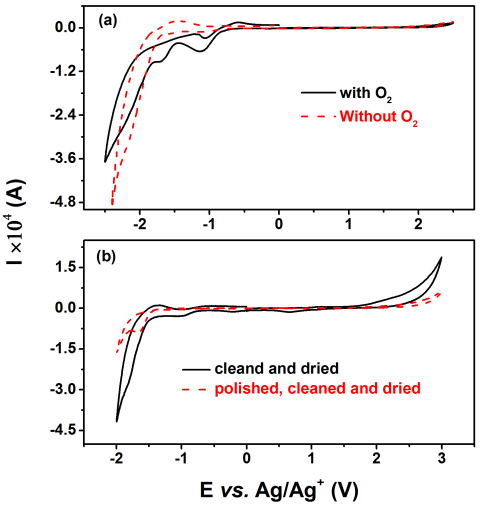

Fig. S14. CV curves showing the influences of (a) dissolved oxygen solution, (b) with/without the working electrode polished before each experiment.

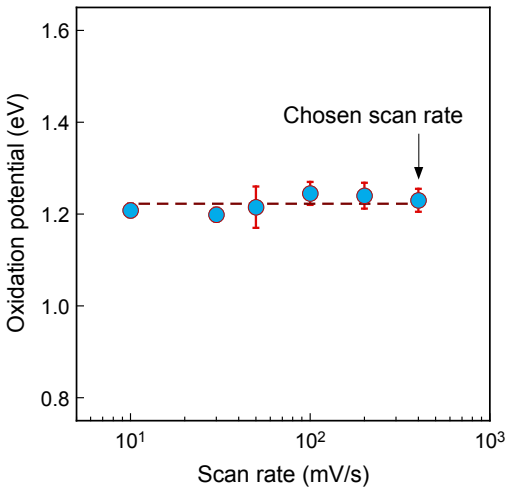

Fig. S15. Effects of voltage scan rate on the oxidation potential. Symbols: experimental data; the line is drawn to guide the eye.

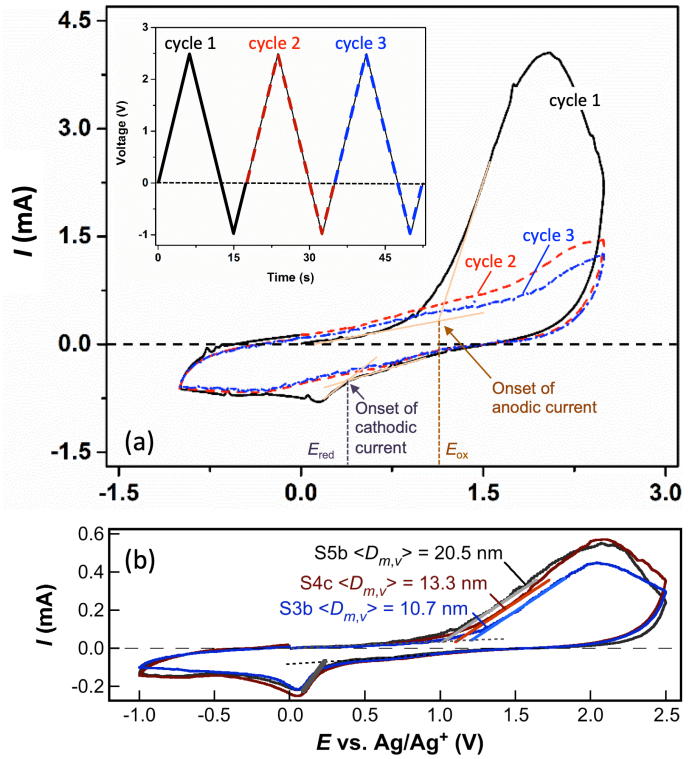

Fig. S16. (a) Cyclic voltammograms of a soot electrode over three cycles of voltage scan. Inset: voltage program. (b) Variation of the oxidation potential E_{ox} as a function of the particle size and the insensitivity of the reduction potential with respect to particle size.

A pair of well-separated anodic and cathodic peaks can be observed in Fig. S16(a) over the first circle. The ratio of anodic to cathodic peak currents is significantly greater than 1, indicating the CNP sample has an appreciable irreversible capacity. The redox signals of second and third circle are very different with those of the first circle; the two peaks disappear due to the electrochemical

irreversibility of the material. The origin of the irreversibility remains unclear at this time. Studies [29-31] have shown that the electron-transfer process and photoluminescence properties are strongly related to the nature of material surfaces [29-31]. A large number of surface functional groups, including phenolic, hydroxyl, and carboxyl functional groups, have been observed for flame-formed CNPs [32-34]. Hence, the irreversibility may be caused by chemical changes of these functional groups during a redox process. Aromatic derivatives may also contribute to the irreversible capacity [30].

Particle size impacts the oxidation potential E_{ox}, but not the reduction potential E_{re}, as shown in Fig. S16*b*. Hence, the electrochemical ionization energy exhibits some size dependence as $\langle E_i^{EC} \rangle$ increases with a decrease in particle size. The electron affinity is, however, found to be insensitive to the particle size.

S7. Effect of Basis Set Size on Calculated HOMO-LUMO Gap

To ensure that the HOMO-LUMO gap calculated for the aromatic clusters is minimally influenced by the basis set size used in the calculation, we carried out a sensitivity analysis on the basis set size. Fig. S17 shows the results obtained for circumcoronene ($C_{54}H_{18}$) and circumcoronaldehyde ($C_{54}H_{18}$-HCO). It can be seen that the HOMO-LUMO gap size is insensitive at or around the basis set size of 6-31G(d), the basis set chosen for the current study.

The gap size is sensitive to composition variations at the molecular level. In particular, functional group substitution of the aromatic molecule has a notable impact on reducing the HOMO-LUMO gap [35]. For example, a single formyl substitution reduces the gap by 0.2 to 0.3 eV.

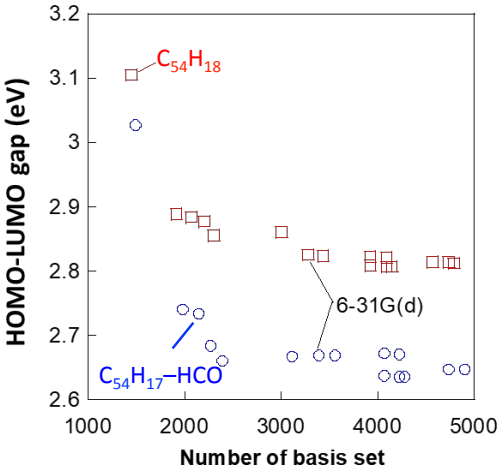

Fig. S17. Impact of basis set size on the prediction of HOMO-LUMO gap of circumcoronene ($C_{54}H_{18}$) w/o single HCO substation.

S7. References

[1] J. Camacho, A.V. Singh, W. Wang, R. Shan, E.K. Yapp, D. Chen, M. Kraft, H. Wang, Soot particle size distributions in premixed stretch-stabilized flat ethylene–oxygen–argon flames, Proc Combust Inst 36 (2017) 1001-1009.

[2] A.E. Lutz, A.E. Kee, J.F. Grear, F.M. Rupley, OPPDIF: A FORTRAN Program for Computing Opposed-Flow Diffusion Flames, Sandia National Laboratories, Livermore, 1997.

[3] H. Wang, X. You, A.V. Joshi, S.G. Davis, A. Laskin, F. Egolfopoulos, C.K. Law, USC Mech Version II. High-Temperature Combustion Reaction Model of H2/CO/C1-C4 Compounds, 2007.

[4] C. Saggese, A.V. Singh, J. Camacho, H. Wang, The distillation curve and sooting propensity of a typical jet fuel, Fuel 235 (2019) 350-362.

[5] A.D. Abid, J. Camacho, D.A. Sheen, H. Wang, Quantitative measurement of soot particle size distribution in premixed flames–the burner-stabilized stagnation flame approach, Combust Flame 156 (2009) 1862-1870.

[6] Z. Li, H. Wang, Drag force, diffusion coefficient, and electric mobility of small particles. I. Theory applicable to the free-molecule regime, Phys Rev E 68 (2003) 061206.

[7] Z. Li, H. Wang, Drag force, diffusion coefficient, and electric mobility of small particles. II. Application, Phys Rev E 68 (2003) 061207.

[8] F.S. Lai, S.K. Friedlander, J. Pich, G.M. Hidy, The self-preserving particle size distribution for Brownian coagulation in the free-molecule regime, J Colloid Interface Sci 39 (1972) 395-405.

[9] M. Schenk, S. Lieb, H. Vieker, A. Beyer, A. Gölzhäuser, H. Wang, K. Kohse-Höinghaus, Imaging nanocarbon materials: Soot particles in flames are not structurally homogeneous, ChemPhysChem 14 (2013) 3248-3254.

[10] M. Schenk, S. Lieb, H. Vieker, A. Beyer, A. Gölzhäuser, H. Wang, K. Kohse-Höinghaus, Morphology of nascent soot in ethylene flames, Proc Combust Inst 35 (2015) 1879-1886.

[11] J. Camacho, C. Liu, C. Gu, H. Lin, Z. Huang, Q. Tang, X. You, C. Saggese, Y. Li, H. Jung, L. Deng, I. Wlokas, H. Wang, Mobility size and mass of nascent soot particles in a benchmark premixed ethylene flame, Combust Flame 162 (2015) 3810-3822.

[12] L.A. Sgro, A. D'Anna, P. Minutolo, Measured charge fraction distributions: information on the formation mechanism of inception mode particles, Combust Flame 158 (2011) 1418-1425.

[13] P. Minutolo, G. Gambi, A. D'Alessio, S. Carlucci, Spectroscopic characterisation of carbonaceous nanoparticles in premixed flames, Atmospheric Environ 33 (1999) 2725-2732.

[14] A. D'Alessio, A.C. Barone, R. Cau, A. D'Anna, P. Minutolo, Surface deposition and coagulation efficiency of combustion generated nanoparticles in the size range from 1 to 10 nm, Proc Combust Inst 30 (2005) 2595-2603.

[15] L.A. Sgro, A.C. Barone, M. Commodo, A. D'Alessio, A. De Filippo, G. Lanzuolo, P. Minutolo, Measurement of nanoparticles of organic carbon in non-sooting flame conditions, Proc Combust Inst 32 (2009) 689-696.

[16] A. D'Alessio, A. D'Anna, G. Gambi, P. Minutolo, The spectroscopic characterization of UV absorbing nanoparticles in fuel rich soot forming flames, J Aerosol Sci 29 (1998) 397-409.

[17] A. D'Alessio, A. D'Anna, P. Minutolo, L. Sgro, Nanoparticles of organic carbon (NOC) formed in flames and their effects in urban atmospheres, in: H. Bockhorn, A. D'Anna, A. Sarofim, H. Wang (Eds.), Combustion Generated Fine Carbonaceous Particles, Karlsruhe University Press, Karlsruhe, 2009, pp. 205-230.

[18] T. Joutsenoja, A. D'Anna, A. D'Alessio, M.I. Nazzaro, Ultraviolet absorption spectra of carbon dioxide and oxygen at elevated temperatures, Appl Spectrosc 55 (2001) 130-135.

[19] D. Cecere, L.A. Sgro, G. Basile, A. D'Alessio, A. D'Anna, P. Minutolo, Evidence and Characterization of Nanoparticles produced in non-Sooting Premixed Flames, Combust Sci Technol 174 (2002) 377-398.
[20] F.-X. Ouf, P. Parent, C. Laffon, I. Marhaba, D. Ferry, B. Marcillaud, E. Antonsson, S. Benkoula, X.-J. Liu, C. Nicolas, First in-flight synchrotron X-ray absorption and photoemission study of carbon soot nanoparticles, Sci Rep 6 (2016) 36495.
[21] L. Brus, Electronic wave functions in semiconductor clusters: experiment and theory, J Phys Chem 90 (1986) 2555-2560.
[22] M. Seidl, J.P. Perdew, Size-dependent ionization energy of a metallic cluster: Resolution of the classical image-potential paradox, Phys Rev B 50 (1994) 5744.
[23] E.A. Davis, N.F. Mott, Conduction in non-crystalline systems V. Conductivity, optical absorption and photoconductivity in amorphous semiconductors, Philos Mag 22 (1970) 0903-0922.
[24] J. Tauc, R. Grigorovici, A. Vancu, Optical properties and electronic structure of amorphous germanium, Phys Status Solidi B 15 (1966) 627-637.
[25] S. Memarzadeh, E.D. Tolmachoff, D.J. Phares, H. Wang, Properties of nanocrystalline TiO2 synthesized in premixed flames stabilized on a rotating surface, Proc Combust Inst 33 (2011) 1917-1924.
[26] G. Basile, A. Rolando, A. D'alessio, A. D'anna, P. Minutolo, Coagulation and carbonization processes in slightly sooting premixed flames, Proc Combust Inst 29 (2002) 2391-2397.
[27] A. Borghese, S.S. Merola, Time-resolved spectral and spatial description of laser-induced breakdown in air as a pulsed, bright, and broadband ultraviolet–visible light source, Appl Opt 37 (1998) 3977-3983.
[28] J. Liu, W. Yang, Y. Li, L. Fan, Y. Li, Electrochemical studies of the effects of the size, ligand and composition on the band structures of CdSe, CdTe and their alloy nanocrystals, Phys Chem Chem Phys 16 (2014) 4778-4788.
[29] X. Wang, L. Cao, S.T. Yang, F. Lu, M.J. Meziani, L. Tian, K.W. Sun, M.A. Bloodgood, Y.P. Sun, Bandgap-like strong fluorescence in functionalized carbon nanoparticles, Angewandte Chemie 49 (2010) 5310-5314.
[30] L. Tian, D. Ghosh, W. Chen, S. Pradhan, X. Chang, S. Chen, Nanosized Carbon Particles From Natural Gas Soot, Chem Mat 21 (2009) 2803-2809.
[31] Z.-h. Yang, H.-q. Wu, Electrochemical intercalation of lithium into fullerene soot, Mat Lett 50 (2001) 108-114.
[32] H. Wang, Formation of nascent soot and other condensed-phase materials in flames, Proc Combust Inst 33 (2011) 41-67.
[33] B. Öktem, M.P. Tolocka, B. Zhao, H. Wang, M.V. Johnston, Chemical species associated with the early stage of soot growth in a laminar premixed ethylene–oxygen–argon flame, Combust Flame 142 (2005) 364-373.
[34] J.P. Cain, P.L. Gassman, H. Wang, A. Laskin, Micro-FTIR study of soot chemical composition—evidence of aliphatic hydrocarbons on nascent soot surfaces, Phys Chem Chem Phys 12 (2010) 5206-5218.
[35] D. Chen, H. Wang, HOMO-LUMO energy splitting in polycyclic aromatic hydrocarbons and their derivatives, Proc Combust Inst 37 (2019) 953-959.